Journal of Materials Chemistry C

ROYAL SOCIETY OF CHEMISTRY

PAPER

View Article Online
View Journal | View Issue

Cite this: J. Mater. Chem. C, 2024, 12, 9139

Discrete and dimeric chiral plasmonic nanorods: intrinsic chirality and extrinsic chirality†

Weiwei Fu,‡[ab] Jiaqi Chen,‡[c] Shunping Zhang,[ad] Guangchao Zheng*[ab] and Yuan Zhang*[ab]

Received 29th March 2024,
Accepted 8th May 2024

DOI: 10.1039/d4tc01258e

rsc.li/materials-c

The recent progress in chemical synthetic methodologies has facilitated the fabrication of discrete plasmonic nanoparticles exhibiting chiral characteristics on their surface. In comparison to conventional gold nanorods (NRs), such structures possess strong plasmonic circular dichroism response, making them highly suitable for various applications involving circularly polarized light. Although the intrinsic and extrinsic chirality of chiral nanostructures produced by the assembly with chiral ligands have been explored both experimentally and theoretically, the investigation into the influencing factors of the intrinsic and extrinsic chirality of discrete chiral Au NRs (dc-Au NRs) has been relatively limited. Herein, we conducted a comprehensive investigation using full-wave electromagnetic simulations to explore the influence of various structural parameters (such as helical depth, width, and numbers of the helical pitches) on the intrinsic and extrinsic chirality of dc-Au NRs. Additionally, we examined the chiral surface plasmon resonance coupling and the corresponding chiral near-field by studying the cross-like assembly of dc-Au NR dimers. These findings serve as valuable guidance for future experimental and theoretical research on chiral plasmonic nanostructures and their applications involving circularly polarized light.

1 Introduction

Plasmonic nanostructures have gained significant attention in various fields of research and application, owing to their exceptionally small mode volume and ability to achieve strong light–matter interaction even at ambient temperatures.[1–3] Under the light excitation, surface plasmon resonance (SPR) can overcome the limitation of optical diffraction and concentrate the electromagnetic field to nanoscale. Thus, the electromagnetic field surrounding plasmonic metal nanoparticles (NPs) is significantly enhanced, leading to surface-enhanced Raman scattering,[4–6] photocatalysis,[7,8] photothermal therapy,[9] and so on. Among these, anisotropic plasmonic NPs, particularly Au nanorods (NRs), exhibit dual SPR peaks along the transverse and the longitudinal axis (TSPR and LSPR), respectively. In comparison to the isotropic metallic NPs, Au NRs exhibit tunable LSPR peaks and enhanced electromagnetic field.[10–12]

Chirality refers to any object that cannot be superimposed onto its mirror image through symmetric operations such as translation or rotation. The chiral object and its mirror-image counterpart are referred to as two enantiomers, which are able to change the incident degree of excited polarized light. Interestingly, the combination of chirality with SPR results in the generation of plasmonic circular dichroism (PCD), which is manifested in the extinction spectra of these systems due to the strong coupling between chiral excitons and SPR.[13–18] Furthermore, the near-field associated with chiral SPR exhibits asymmetry and dependence on circular polarization, distinguishing from the near-field surrounding achiral metal nanostructures.[19–23] Later, by merit of the chiral near-field, numerous circular-polarization applications have been demonstrated, such as asymmetric photocatalysis,[24–26] enantiomeric sensing or surface-enhanced Raman scattering,[27–30] cancer therapy,[31–33] *etc.* There are two types of chirality involving intrinsic chirality and extrinsic chirality based on the sensitivity of chiral response to the oblique light.[34–38] While the intrinsic chirality is insensitive to the change of incident light, the extrinsic chirality varies significantly when the incident light changes at certain angles. Due to advances in the synthetic methodologies in wet-chemistry, discrete chiral metallic nanostructures exhibiting strong chiroptical response, stability and durability have been fabricated in world-famous labs.[39–46] While the chiral response of discrete

[a] Key laboratory of Material Physics, Ministry of Education, School of Physics and Microelectronics, Zhengzhou University, Zhengzhou, 450001, China. E-mail: gczheng@zzu.edu.cn, yzhuaudipc@zzu.edu.cn
[b] Institute of Quantum Materials and Physics, Henan Academy of Sciences, Zhengzhou 450046, China
[c] School of Mechanical Engineering, Chengdu University, Chengdu 610000, China
[d] Center for Nanoscience and Nanotechnology, and School of Physics and Technology, Wuhan University, Wuhan 430072, China

† Electronic supplementary information (ESI) available. See DOI: https://doi.org/10.1039/d4tc01258e

‡ These authors contributed equally to this work.

chiral nanostructures is often attributed to the chiral surface features, the spectra measured experimentally often suffer from the ensemble average effect due to the inhomogeneous shapes of the synthesized nanoparticles and their random orientations with respect to the probe beam. Thus, it is imperative to undertake a comprehensive study on the intrinsic and extrinsic chirality of discrete chiral nanostructures and analyze how the intrinsic chirality can be preserved in the presence of ensemble average.

Recently, several groups have tried to obtain dimers of discrete chiral nanostructures in order to reveal the coupling of chiral SPR.[47,48] In one of our previous works,[49] we developed seed-mediated growth methods using the amino thiols and L-cysteine (L-cys) or D-cysteine (D-cys) for the fabrication of discrete chiral Au NRs (dc-Au NRs), and built a simple model of dc-Au NRs. Yang *et al.* have fabricated the AuCu chiral hetero-nanostructures using the discrete chiral Au nanoparticles as the seeds. By controlling the experimental parameters, Cu nanodomains were selectively grown on the tips of discrete chiral Au nanoparticles. The authors simulated the near-field enhancements of AuCu chiral hetero-nanostructures.[45] Zhou and his colleagues have studied the chiroptical performance of assembled dc-Au NRs with DNA origami experimentally.[48] Unfortunately, restricted by the thickness of DNA origami, the interparticle distance between two dc-Au NRs exceeded several tens of nanometers, weakening the coupling of their chiral SPR that they claimed in their work. In our previous work, we have obtained the side-by-side assembly of dc-Au NRs, exhibiting enhanced chiroptical response and blue-shifted PCD peaks.[15] However, despite the significant progress in the field of dc-Au NRs, detailed studies on the influence of structural parameters on the chiroptical responses of distinct and assembled dc-Au NRs are still lacking. In addition, the understanding of intrinsic and extrinsic chirality based on the discrete and self-assembled dc-Au NRs need to be further demonstrated. Furthermore, the comprehensive experimental and theoretical investigations into the coupling of chiral SPR should be strengthened.

Herein, we carry out a systematic study on the dependence of structural parameters (*e.g.*, light incidence, helical depth, width and turning number of the helical pitches) on the intrinsic and extrinsic chirality of dc-Au NRs through full-wave electromagnetic simulations. Then, the 3D cross-like assembly of dc-Au NR dimers is studied for the chiral SPR coupling and the derived chiral near-field. Our results provide insights into the structure–performance relationship and can guide the rational design and application of chiral metallic nanostructures.

2 Experiment and theory

2.1 Synthesis and PCD of dc-Au NRs

In our experiment, we follow the protocol reported in our earlier studies to control the generation of chiral morphology of Au NRs by using L-cys and D-cys molecules (Fig. 1a), and present the detailed experimental procedures in the ESI.† Transmission electron microscopy (TEM) images clearly depict the presence of chiral features on the surface of the synthesized dc-Au NRs. Specifically, the utilization of the L-cys (D-cys) molecules results in the chiral growth of a left-handed (right-handed) geometry on the surface (Fig. 1b) and thus will be denoted as L-Au NR (D-Au NR) in the following. The measured extinction spectra show similar features of both types of NRs with double peaks around 520 nm and 780 nm (Fig. 1c), which can be attributed to TSPR and LSPR, respectively. The measured PCD spectra show the typical bisignate features around the wavelengths of these SPR with negative and positive couplets for the L-Au NR and D-Au NR (Fig. 1d). In addition, we note that the PCD peaks at the wavelength of the TSPR are slightly larger than those at the wavelength of the LSPR.

2.2 Theoretical model of dc-Au NRs

To understand the PCD of dc-Au NRs, we carry out full-wave electromagnetic simulations by using the commercial COMSOL

Guangchao Zheng

Guangchao Zheng obtained his MSc degree from the University of Science and Technology of China in 2012. He received his PhD degree in 2015 from the University of Vigo (Spain) under the supervision of Professors Jorge Perez-Juste and Luis M. Liz-Marzan. Then he worked as a research associate (2016–2017) and research fellow (2017–2019) in the Hong Kong Polytechnic University. He has served as an Associate Professor and established the Colloidal Physics group at the Zhengzhou University (China) since 2019. The scope of his research focuses on the structure-oriented application of colloidal nanoparticles, surface-enhanced spectroscopy (SERS/SEF), photocatalysis, bio-applications and chiral nanophotonics.

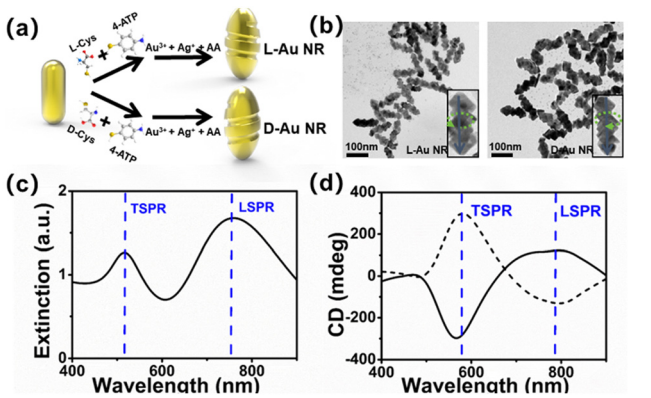

Fig. 1 Morphology and characterization of dc-Au NRs. (a) Schematic diagram of growth procedure of L-Au NR and D-Au NR using L-cys and D-cys molecules, respectively. (b) TEM images of synthesized L-Au NR (i) and D-Au NR (ii), showing right- and left-helical features on the metal surface (inset), respectively. (c) and (d) Measured extinction spectra (c), and PCD spectra (d) of L-Au NR (solid line) and D-Au NR (dashed line).

software, which solves the Maxwell's equation using the finite-element method, and utilizes the Au dielectric function from the experimental data of Johnson and Christy.[50] More details on the COMSOL modeling are provided in Fig. S1 (ESI†). The extinction cross-section $A_{ext} = A_{sc} + A_{abs}$ is the sum of the scattering cross-section A_{sc} and the absorption cross-section A_{abs}. The former $A_{sc} = \frac{1}{I_0}\int\int_S S_{sc} ds$ can be calculated by integrating the Poynting vector S_{sc} of the scattered light over a surface s around the nanoparticle, and the latter $A_{abs} = \int\int\int Q dV$ can be calculated by integrating the power loss intensity Q over the volume V of the nanoparticle. Here, I_0 is the intensity of the incident light. From the extinction cross-section $A^L_{ext} - A^R_{ext}$ for the left- and right-polarized incident light, we can determine the circular dichroism as their difference CD = A^L_{ext}, A^R_{ext}.

3 Results

3.1 Influence of NR orientations relative to light incidence

The measured extinction and PCD spectra, as shown in Fig. 1c and d, do not directly correspond to those of dc-Au NRs (although highly desired), and suffer actually from the ensemble average due to the inhomogeneity of the synthesized NRs, and more importantly the random orientation of dc-Au NRs with respect to the incidence of the left-/right-polarized light. To illustrate the latter point, in Fig. 2, for the case of D-Au NR, we study theoretically the dependence of the extinction and PCD spectra on the orientation of the dc-Au NRs relative to the incidence of the left-/right-polarized light. Similar results for the L-Au NR are shown in Fig. S2 (ESI†).

To understand the results, we can project the light polarization onto the direction parallel and perpendicular to the long axis of the Au NRs and find that the projections do not depend on the azimuth angle φ but critically on the polar angle θ (Fig. S3, ESI†). More precisely, the projection along the NR long axis increases as the angle θ approaches 90°. As a result, for a given θ and varying φ, we do not observe significant changes in the extinction and PCD spectra (not shown). In contrast, for given φ = 0° and increasing θ from 0° to 90°, we observe the significant increase of the extinction and PCD at the LSPR wavelength, and the unchanged results at the TSPR wavelength (Fig. 2b and c), all of which can be attributed to the increased excitation of the LSPR mode with the enhanced field along the NR long axis. By integrating the spectra for the angle θ = 0°,···180°, φ = 0°,···360°, we obtain the orientation-averaged extinction and PCD spectra (Fig. 2d and e). These results are consistent with the experimentally measured results (Fig. 1c and d). This result suggests the importance of the orientation-averaged effect in the interpretation of the experimental results, and such an effect might be verified using more advanced techniques to detect the chiral response of single-metallic nanostructures in the future. In addition, we also find that the width of the peaks and dips in the simulation is much narrower than that in the experiment, which can be attributed to the influence of the geometric inhomogeneity of NR, especially the change of the aspect ratio of NR. Note that the LSPR wavelength is very sensitive to the aspect ratio, as confirmed using the simulated extinction and PCD spectra for dc-Au NRs with different aspect ratios (Fig. S4, ESI†). It can be found that, with the increase of the aspect ratio, the TSPR almost remains almost unchanged, but the LSPR red-shifts dramatically. In addition, the LSPR also red-shifts in the PCD spectra, but its intensity does not change significantly. This also confirms that the chirality of dc-Au NRs comes from the intrinsic chirality and the extrinsic chirality merely changes the response strength.

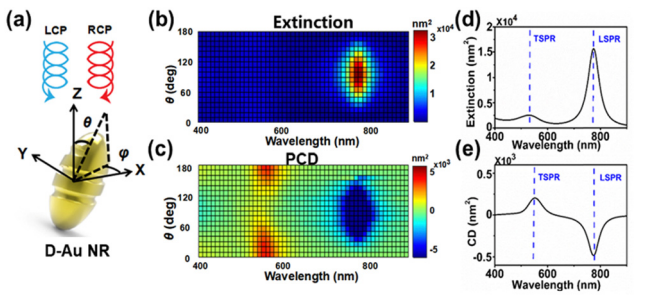

Fig. 2 Influence of orientation of D-Au NR to the light incidence on the PCD response. (a) Schematic of the incident left-/right-polarized light along the negative z-axis, and the dc-Au NRs with orientation specified by the polar angle θ and azimuth angle φ. The NRs have a length of 57.5 nm and half-axis of 20 nm along the short axis, respectively, and the chiral feature on the surface has a radius of 15 nm and a helical depth about 10 nm. (b) and (c) Calculated extinction (b) and PCD (c) spectra for θ = 0°, 10°, 20°···180° and φ = 0°. The results for fixed θ do not show significant dependence on the angle φ. (d) and (e) Calculated extinction (d) and PCD (e) spectra by integrating the spectra for the angle θ = 0°,···180°, φ = 0°,···360°, which resemble the experimental results shown in Fig. 1c and d.

3.2 Influence of the chiral surface of Au NRs

In the above simulations, we find that the averaged extinction spectra and the PCD spectra are very similar to the Au NR spectra with the light incidence angle θ = 45°. Thus, we can calculate all the spectra under such illumination conditions in the following simulations, in order to estimate orientation-averaged results qualitatively, as measured in the experiment. Since the PCD of dc-Au NRs mainly arises from the chiral feature on the metal surface, it is necessary to understand how the geometry of this feature affects their PCD performance (Fig. 3). The model of dc-Au NRs with typical thread grooves is specified in Fig. 3a. Then, the effect of structure parameters (*i.e.*, depth (d), width (w) and turn number (n) of grooves) on the extinction and PCD spectra of dc-Au NRs are systematically investigated). Upon increasing n of the helical pitches, we observed minimal changes in the extinction spectra (Fig. S5, ESI†) and a slight weakening of the PCD spectra (Fig. 3b) at longer wavelengths as well as the constant PCD at shorter wavelengths. In order to better study the effect of structural parameters on the optical activity, we increase the width of the groove, w from 28 nm to 32 nm. As a result, the extinction due to LSPR has a significant blue-shift from 820 nm to 750 nm (Fig. 3c), and the extinction due to TSPR has a red-shift. At the same time, the dips or peaks of PCD also show a blue-shift, and the intensity of PCD weakens significantly (Fig. 3d). When the

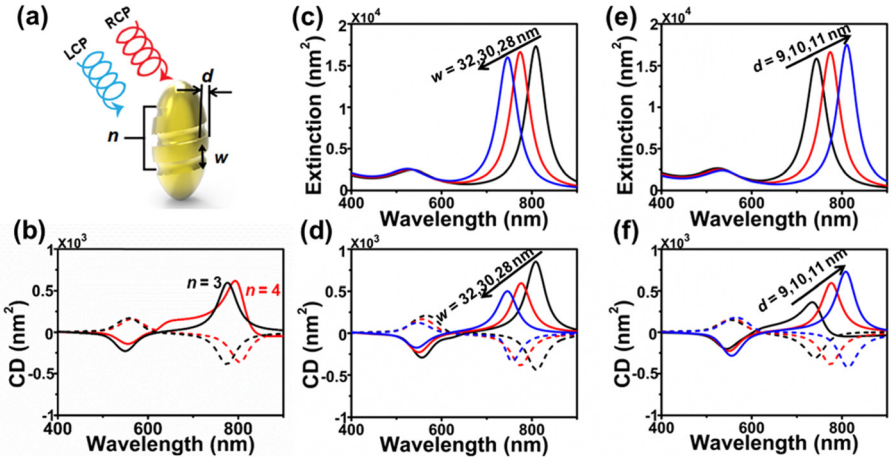

Fig. 3 Influence of chiral feature on Au NRs surface on PCD response. (a) Schematic of thread grooves on Au NRs surface, specified by the groove depth d, width w, and turning number n. (b) Calculated PCD for d = 10 nm, w = 30 nm and increasing n = 3, 4 (red and black lines). (c) and (d) Calculated extinction (c) and PCD spectra (d) for n = 3, d = 10 nm, and increasing w = 28, 30, 32 nm (black, red and blue lines). (e) and (f) Calculated extinction (e) and PCD spectra (f) for w = 30 nm, n = 3, and increasing d = 9, 10, 11 nm (black, red and blue lines). In (c) and (d) and remaining panels, the solid and dashed lines represent the NRs with left- and right-handed surfaces. Here, the incident light forms an angle of 45° with respect to the long axis of the NR.

groove depth d increases from 9 nm to 11 nm, the extinction and PCD due to LSPR become red-shifted and enhanced, while those due to TSPR almost remain constant (Fig. 3e and f). If these dc-Au NRs are equated with smooth-surfaced Au NRs, we expect that the increase in the groove depth and the decrease in the groove width not only increase the effective aspect ratio of NR, but also make the chiral characteristics more pronounced, which explains the red-shift of LSPR as well as the increase in intensity. In addition, in Fig. S6 (ESI†), we present the spectra of the achiral Au NRs with the smooth surface and observe the blue-shift of the LSPR and no obvious optical activity. Therefore, the helical feature on the surface of dc-Au NRs causes the red-shift of LSPR and the appearance of the PCD response, *i.e.* the domination of the intrinsic chirality.

3.3 Chiral SPR coupling of assembled dc-Au NRs

The above simulations provide important insights into the PCD response of dc-Au NRs. Experimentally, we can also synthesize dimers by coupling two dc-Au NRs for the further investigation on their chiral SPR coupling. More TEM images and experimental results of this structure are shown in Fig. S7 and S8 of the ESI.† Using appropriate screening techniques, it will be possible to obtain a collection of such dimers in the future. Compared with dc-Au-NRs, the self-assembled dc-Au NRs can form hybrid plasmons through near-field coupling, and the SPR can be tuned over a larger wavelength range by controlling the relative positions of the NRs. In addition, in the past decade, 3D chiral structures constructed with assembly of DNA or DNA origami templates have become very mature, but most of their basic constructed metallic units are non-chiral. There are a few research studies on 3D chiral structures constructed *via* assembly of metal plasmonic NRs with intrinsic chirality. Zhou *et al.* recently have successfully produced such a 3D structure *via* assembly of dc-Au NRs with DNA origami.[48]

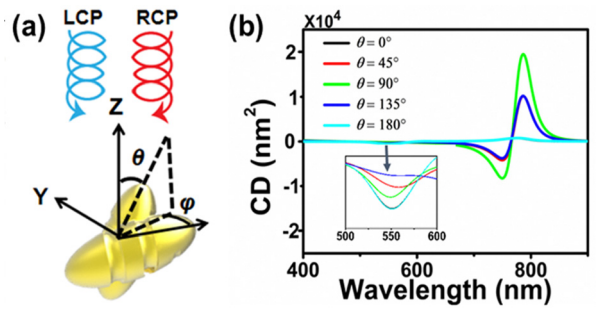

Fig. 4 Influence of illumination conditions on the PCD performance of self-assembled dc-Au NRs. (a) Schematic of the incident left-/right-polarized light along the negative z-axis, and self-assembled dc-Au NRs with orientation specified by the polar angle θ and azimuth angle φ. (b) Simulated PCD spectra of those dc-Au NR dimers for θ = 0°, 45°,···180° and given φ = 90°.

Inspired by these studies, we construct an equivalent model, as shown in Fig. 4a. The angle between the two L-Au NRs is 45°. We can project the light polarization to the direction parallel and perpendicular to long axis of the Au NRs and find that different azimuth angles φ and polar angles θ have different effects on the PCD spectra, which indicated the greater sensitivity of the PCD of dimeric structures. As an example, we consider the azimuth angle φ = 90°, and the polar angle θ = 0°,45°,···180°. At the polar angle θ = 0° or θ = 180°, the incident light is parallel to the self-assembled dc-Au NRs, which leads to the dominance of intrinsic chirality, the PCD of self-assembled dc-Au NRs is similar to that of dc-Au NR. When polar angle θ = 45°, 90°, 135°, the symmetry of the system composed of self-assembled dc-Au NRs and oblique incident light is disrupted, resulting in the formation of extrinsic chirality. Thus, the PCD spectra show obvious extrinsic chirality (Fig. 4b). As shown in Fig. S9 (ESI†), the similar peaks and dips occur for the dimers of achiral Au NRs, which indicates the dominance of the external PCD. In addition, the difference between partial

enlarged drawing at 500–600 nm confirms the existence of intrinsic chirality. When we keep the polar angle θ unchanged and change azimuth angle φ, we find that the PCD result is consistent with Fig. 4b. In addition, we find that for the polar angle $\theta = 0^\circ$ and the azimuth angle $\varphi = 0^\circ$, the results were very similar to Zhou's experiment. In order to better compare with Zhou's experimental results, we calculate spectra under this illumination conditions in the following simulations.

As illustrated in Fig. 5a, for better description, we classified the assembled chiral structure "DH" (dexter-handed) and "LH" (laevus-handed) according to the direction of vertical incidence of light, *i.e.* the clockwise and counterclockwise rotation direction of the dc-Au NRs, respectively. They are composed of two L-Au NRs or two D-Au NRs, separated by distance S. Here, the center–center distance $S = 44$ nm corresponds to a gap distance (G) of 4 nm (Fig. S10, ESI†). The angle between the two dc-Au NRs is 45°. Fig. 5b and c show the extinction spectra and PCD spectra for self-assembled dc-Au NRs with gap distance 40 and 4 nm. From the extinction spectra of the latter system, we can see four resonance peaks at 520 nm (λ_1), 620 nm (λ_2), 750 nm (λ_3) and 820 nm (λ_4).

To illustrate the nature of the SPR at these wavelengths, Fig. 5e (Fig. S11, ESI†) shows the corresponding electric field distribution at wavelengths λ_3, λ_4, (λ_1, λ_2) for the DH/LH. For illuminations at λ_1, λ_2, the electric field of the whole particle is almost zero, and it only has value on the edges of the groove. Since the surface electric field distribution of self-assembled dc-Au NRs does and does not concentrate at the gap shown in the Fig. S11a and b, ESI,† respectively, the corresponding plasmons can be attributed to the transverse plasmon of individual particles, and the transverse plasmon of coupled particles. In contrast, the electric field is relatively larger through the body, and becomes zero at some parts of groove edges for the illumination at λ_3, λ_4 (Fig. 5e). A dc-Au NR firstly was regarded as a dipole, according to the plasmon hybridization theory, when two dc-Au NRs are separated by a few nanometers, their SPR will become strong coupling leading to generation of two hybrid resonance modes with different energies.[51] One mode is low-energy bonding mode corresponding to λ_4, and another mode is a high-energy anti-bonding mode corresponding to λ_3 (Fig. 5d). These hybridized modes represent the symmetric and asymmetric combination of two dipolar plasmon resonances. When the wavelength is λ_3, LCP and RCP in the same structure show obvious symmetrical electric field distribution and strong dipolarity, while in LCP (RCP), DH structure and LH structure show horizontal mirror symmetry, which is a feature of the anti-bonding mode (panel (i) in Fig. 5c). For λ_4, LCP and RCP exhibit obvious asymmetric distribution under the same structure, and the LH (DH) structure under LCP and the DH (LH) structure under RCP exhibit vertical mirror symmetry, which is a characteristic of the bonding mode (panel (ii) in Fig. 5c).[47] As shown in Fig. S12 (ESI†), the same electric field is observed in the dimers of the achiral Au NRs, which indicates the dominance of the external PCD here. From the PCD spectra in Fig. 5c, we can also see the four resonant peaks, and mirror symmetry for both configurations. Note that the PCD here is much stronger than that for individual particles. In addition, we also demonstrate the surface charge distribution of self-assembled dc-Au NRs, which is very similar to the electric field distribution (Fig. S13, ESI†).

In the Fig. S14 (ESI†), we show the extinction spectra and PCD spectra at different separations G. As G increases, the coupling between the two dc-Au NRs weakens, and the PCD at λ_2 decreases and disappears eventually. In addition, the

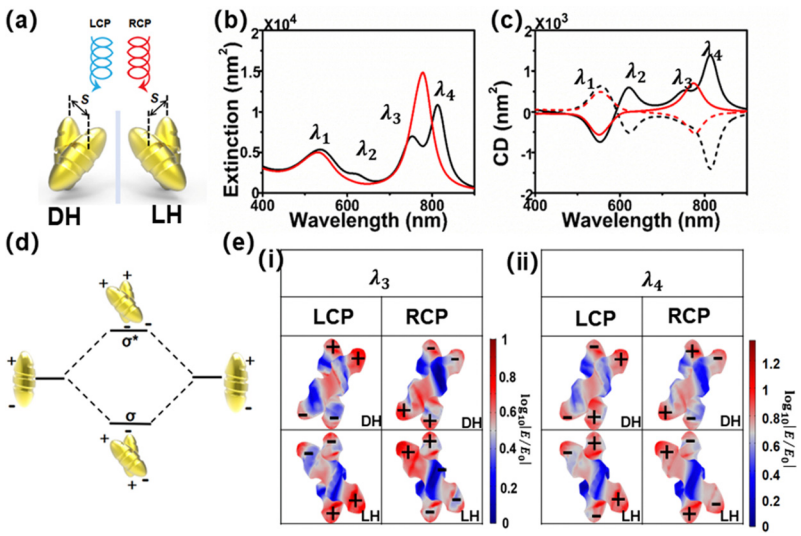

Fig. 5 Chiral response of self-assembled dc-Au NRs. (a) Schematic diagram of the self-assembled dc-Au NRs, where the left-handed and right-handed configuration are named as LH and DH, respectively. (b) and (c) Show the extinction spectra and PCD spectra for self-assembled dc-Au NRs with distance $S = 80$, 44 nm (red and black lines). Here, the distance S refers to the center-center distance between two nanorods, and the actual gap distance $G = S - 2 \times D$ can be achieved by subtracting two times of the short-axis radius D. The solid and dashed lines represent the DH/LH, and the incident light forms an angle of 0° with respect to the long axis of the NR. (d) Diagrams of bonding mode and anti-bonding mode. (e) Electric field distribution of the DH and LH structures for the bonding mode and anti-bonding mode.

difference between λ_3 and λ_4 becomes smaller. For G = 40 nm, the feature at λ_3 disappears and that at λ_4 becomes blue-shifted and its intensity decreases, which is consistent with Zhou's experimental results (Fig. 3 of ref. 48). Furthermore, we have also studied the DH composed of two D-Au NRs and the LH composed of two L-Au NRs in the Fig. S14c (ESI†). After comparison of the PCD spectra, we confirm again that the PCD at λ_1 is mainly determined by the intrinsic chirality of the composed dc-Au NRs, while the PCD at λ_3 and λ_4 is determined by extrinsic chirality.

4 Conclusions

In this manuscript, we have synthesized dc-Au NRs using the seed growth method assisted by L-cys and D-cys molecules and characterized their morphology with TEM and their optical response with extinction and PCD spectra. By modeling these dc-Au NRs with full-wave electromagnetic simulations, we studied theoretically the influence of the NR orientation, and reproduced qualitatively the experimental results, highlighting the importance of the ensemble average effect. By changing the geometry of grooves, we found that the red-shift of extinction peaks and PCD responses corresponding to LSPR can be roughly attributed to the modified effective aspect ratio, and the chiral feature with a large size would lead to the more pronounced chiral response. Furthermore, by coupling two dc-Au NRs, the PCD feature became richer due to the formation of hybrid plasmon modes, and this feature can be actively tuned by controlling the relative positions of the two NRs. All in all, our study provided insights into the origin of PCD from chiral feature on the metal surface, and the interplay of PCD with those due to arrangement of coupled chiral NRs. As a result, it might guide further experimental and theoretical studies in this research direction.

Author contributions

W. Fu and J. Chen: investigation, data curation, analysis, writing, and funding; S. Zhang: writing–review and editing, G. C. Zheng and Y. Zhang: supervision, methodology, writing–review and editing, and funding. All authors have given approval to the final version of the manuscript.

Conflicts of interest

There are no conflicts to declare.

Acknowledgements

This work was supported by the National Natural Science Foundation of China (Grants No. 22271257, 12004344, and 21902148) and the Sichuan Natural Science Foundation Project (24NSFSC2668).

Notes and references

1 L. Scarabelli, M. Sun, X. Zhuo, S. Yoo, J. E. Millstone, M. R. Jones and L. M. Liz-Marzán, *Chem. Rev.*, 2023, **123**, 3493–3542.
2 A. Kuzyk, R. Schreiber, Z. Fan, G. Pardatscher, E.-M. Roller, A. Högele, F. C. Simmel, A. O. Govorov and T. Liedl, *Nature*, 2012, **483**, 311–314.
3 G. Zheng, S. Mourdikoudis and Z. Zhang, *Small*, 2020, **16**, 2002588.
4 J. F. Li, Y. F. Huang, Y. Ding, Z. L. Yang, S. B. Li, X. S. Zhou, F. R. Fan, W. Zhang, Z. Y. Zhou, D. Y. Wu, B. Ren, Z. L. Wang and Z. Q. Tian, *Nature*, 2010, **464**, 392–395.
5 S. Lin, H. Ze, X.-G. Zhang, Y.-J. Zhang, J. Song, H. Zhang, H.-L. Zhong, Z.-L. Yang, C. Yang, J.-F. Li and Z. Zhu, *Angew. Chem., Int. Ed.*, 2022, **61**, e202203511.
6 G. Zheng, J. Wang, L. Kong, H. Cheng and J. Liu, *Plasmonics*, 2012, **7**, 487–494.
7 Y. Yang, C. Hu, J. Shan, C. Cheng, L. Han, X. Li, R. Wang, W. Xie, Y. Zheng and T. Ling, *Angew. Chem., Int. Ed.*, 2023, **62**, e202300989.
8 X. Fu, S. Wang, S. Mourdikoudis, J. Sun, X. Liu, W. Fu, Y. Zhang, F. Ma, L. Er-Jun and G. Zheng, *ACS Sustainable Chem. Eng.*, 2022, **11**, 29–37.
9 J.-S. Lin, X.-D. Tian, G. Li, F.-L. Zhang, Y. Wang and J.-F. Li, *Chem. Soc. Rev.*, 2022, **51**, 9445–9468.
10 J. Zheng, X. Cheng, H. Zhang, X. Bai, R. Ai, L. Shao and J. Wang, *Chem. Rev.*, 2021, **121**, 13342–13453.
11 H. Chen, L. Shao, Q. Li and J. Wang, *Chem. Soc. Rev.*, 2013, **42**, 2679–2724.
12 J. Ye, Q. Wen, Y. Wu, Q. Fu, X. Zhang, J. Wang, S. Gao and J. Song, *Nano Res.*, 2022, **15**, 6372–6398.
13 J. Lu, Y. Xue, K. Bernardino, N. N. Zhang, W. R. Gomes, N. S. Ramesar, S. Liu, Z. Hu, T. Sun, A. F. de Moura, N. A. Kotov and K. Liu, *Science*, 2021, **371**, 1368–1374.
14 X. Lan, X. Lu, C. Shen, Y. Ke, W. Ni and Q. Wang, *J. Am. Chem. Soc.*, 2015, **137**, 457–462.
15 G. Zheng, Z. Bao, J. Pérez-Juste, R. Du, W. Liu, J. Dai, W. Zhang, L. Y. S. Lee and K.-Y. Wong, *Angew. Chem., Int. Ed.*, 2018, **57**, 16452–16457.
16 G. Zheng, J. He, V. Kumar, S. Wang, I. Pastoriza-Santos, J. Pérez-Juste, L. M. Liz-Marzán and K. Y. Wong, *Chem. Soc. Rev.*, 2021, **50**, 3738–3754.
17 Q. Gao, L. Tan, Z. Wen, D. Fan, J. Hui and P.-P. Wang, *Nano Res.*, 2023, **16**, 11107–11124.
18 Y. He, H. Li, A. M. Steiner, A. Fery, Y. Zhang and C. Ye, *Adv. Mater.*, 2023, e2303595.
19 M. Schäferling, X. Yin, N. Engheta and H. Giessen, *ACS Photonics*, 2014, **1**, 530–537.
20 E. Petronijevic, E. M. Sandoval, M. Ramezani, C. L. Ordóñez-Romero, C. Noguez, F. A. Bovino, C. Sibilia and G. Pirruccio, *J. Phys. Chem. C*, 2019, **123**, 23620–23627.
21 A. Movsesyan, A. Muravitskaya, L. V. Besteiro, E. Y. Santiago, O. Ávalos-Ovando, M. A. Correa-Duarte, Z. Wang, G. Markovich and A. O. Govorov, *Adv. Opt. Mater.*, 2023, **11**, 2300013.

22 L. Hu, Z. Sun, Y. Nie, Y. Huang and Y. Fang, *Laser Photonics Rev.*, 2022, **16**, 2200035.
23 W. Du, X. Wen, D. Gérard, C.-W. Qiu and Q. Xiong, *Sci. China-Phys. Mech. Astron.*, 2019, **63**, 244201.
24 Y. Negrín-Montecelo, A. Movsesyan, J. Gao, S. Burger, Z. M. Wang, S. Nlate, E. Pouget, R. Oda, M. Comesaña-Hermo, A. O. Govorov and M. A. Correa-Duarte, *J. Am. Chem. Soc.*, 2022, **144**, 1663–1671.
25 W. Fu, L. Tan and P.-P. Wang, *ACS Nano*, 2023, **17**, 16326–16347.
26 O. Ávalos-Ovando, E. Y. Santiago, A. Movsesyan, X.-T. Kong, P. Yu, L. V. Besteiro, L. K. Khorashad, H. Okamoto, J. M. Slocik, M. A. Correa-Duarte, M. Comesaña-Hermo, T. Liedl, Z. Wang, G. Markovich, S. Burger and A. O. Govorov, *ACS Photonics*, 2022, **9**, 2219–2236.
27 R. M. Kim, J.-H. Huh, S. Yoo, T. G. Kim, C. Kim, H. Kim, J. H. Han, N. H. Cho, Y.-C. Lim, S. W. Im, E. Im, J. R. Jeong, M. H. Lee, T.-Y. Yoon, H.-Y. Lee, Q. H. Park, S. Lee and K. T. Nam, *Nature*, 2022, **612**, 470–476.
28 M. Arabi, A. Ostovan, Y. Wang, R. Mei, L. Fu, J. Li, X. Wang and L. Chen, *Nat. Commun.*, 2022, **13**, 5757.
29 G. Wang, C. Hao, W. Ma, A. Qu, C. Chen, J. Xu, C. Xu, H. Kuang and L. Xu, *Adv. Mater.*, 2021, **33**, 2102337.
30 Z. Liu, J. Ai, P. Kumar, E. You, X. Zhou, X. Liu, Z. Tian, P. Bouř, Y. Duan, L. Han, N. A. Kotov, S. Ding and S. Che, *Angew. Chem. Int. Ed.*, 2020, **59**, 15226–15231.
31 J. Yeom, P. P. G. Guimaraes, H. M. Ahn, B.-K. Jung, Q. Hu, K. McHugh, M. J. Mitchell, C.-O. Yun, R. Langer and A. Jaklenec, *Adv. Mater.*, 2020, **32**, 1903878.
32 C. Ma, P. Yu, W. Wang, Y. Zhu, F. Lin, J. Wang, Z. Jing, X.-T. Kong, P. Li, A. O. Govorov, D. Liu, H. Xu and Z. Wang, *ACS Nano*, 2021, **15**, 16357–16367.
33 F. Gao, M. Sun, W. Ma, X. Wu, L. Liu, H. Kuang and C. Xu, *Adv. Mater.*, 2017, **29**, 1606864.
34 M. Qiu, L. Zhang, Z. Tang, W. Jin, C.-W. Qiu and D. Y. Lei, *Adv. Funct. Mater.*, 2018, **28**, 1803147.
35 U. Hananel, A. Ben-Moshe, D. Tal and G. Markovich, *Adv. Mater.*, 2020, **32**, 1905594.
36 C. Wang, Z. Li, R. Pan, W. Liu, H. Cheng, J. Li, W. Zhou, J. Tian and S. Chen, *ACS Photonics*, 2020, **7**, 3415–3422.
37 N. Kowalska, F. Bandalewicz, J. Kowalski, S. Gómez-Graña, M. Bagiński, I. Pastoriza-Santos, M. Grzelczak, J. Matraszek, J. Pérez-Juste and W. Lewandowski, *ACS Appl. Mater. Interfaces*, 2022, **14**, 50013–50023.
38 M. Hentschel, M. Schäferling, X. Duan, H. Giessen and N. Liu, *Sci. Adv.*, 2017, **3**, e1602735.
39 L. Xu, X. Wang, W. Wang, M. Sun, W. J. Choi, J. Y. Kim, C. Hao, S. Li, A. Qu, M. Lu, X. Wu, F. M. Colombari, W. R. Gomes, A. L. Blanco, A. F. de Moura, X. Guo, H. Kuang, N. A. Kotov and C. Xu, *Nature*, 2022, **601**, 366–373.
40 B. Ni, M. Mychinko, S. Gómez-Graña, J. Morales-Vidal, M. Obelleiro-Liz, W. Heyvaert, D. Vila-Liarte, X. Zhuo, W. Albrecht, G. Zheng, G. González-Rubio, J. M. Taboada, F. Obelleiro, N. López, J. Pérez-Juste, I. Pastoriza-Santos, H. Cölfen, S. Bals and L. M. Liz-Marzán, *Adv. Mater.*, 2023, **35**, 2208299.
41 G. González-Rubio, J. Mosquera, V. Kumar, A. Pedrazo-Tardajos, P. Llombart, D. M. Solís, I. Lobato, E. G. Noya, A. Guerrero-Martínez, J. M. Taboada, F. Obelleiro, L. G. MacDowell, S. Bals and L. M. Liz-Marzán, *Science*, 2020, **368**, 1472–1477.
42 H.-E. Lee, H.-Y. Ahn, J. Mun, Y. Y. Lee, M. Kim, N. H. Cho, K. Chang, W. S. Kim, J. Rho and K. T. Nam, *Nature*, 2018, **556**, 360–365.
43 G. Zheng, S. Jiao, W. Zhang, S. Wang, Q. Zhang, L. Gu, W. Ye, J. Li, X. Ren, Z. Zhang and K.-Y. Wong, *Nano Res.*, 2022, **15**, 6574–6581.
44 Q. Cheng, J. Yang, L. Sun, C. Liu, G. Yang, Y. Tao, X. Sun, B. Zhang, H. Xu and Q. Zhang, *Nano Lett.*, 2023, **23**, 11376–11384.
45 G. Z. Yang, L. C. Sun, Y. L. Tao, Q. Q. Cheng, X. H. Sun, C. Liu and Q. F. Zhang, *Sci. China: Chem.*, 2023, **66**, 3280–3289.
46 N.-N. Zhang, H.-R. Sun, Y. Xue, F. Peng and K. Liu, *J. Phys. Chem. C*, 2021, **125**, 10708–10715.
47 L. Zhang, Y. Chen, J. Zheng, G. R. Lewis, X. Xia, E. Ringe, W. Zhang and J. Wang, *Angew. Chem., Int. Ed.*, 2023, **62**, e202312615.
48 J. Pan, X. Wang, J. Zhang, Q. Zhang, Q. Wang and C. Zhou, *Nano Res.*, 2022, **15**, 9447–9453.
49 J. Chen, X. Gao, Q. Zheng, J. Liu, D. Meng, H. Li, R. Cai, H. Fan, Y. Ji and X. Wu, *ACS Nano*, 2021, **15**, 15114–15122.
50 P. B. Johnson and R. W. Christy, *Phys. Rev. B: Solid State*, 1972, **6**, 4370–4379.
51 E. Prodan, C. Radloff, N. J. Halas and P. Nordlander, *Science*, 2003, **302**, 419–422.